Improved qubit bifurcation readout in the straddling regime of circuit QED

Maxime Boissonneault,[1],[*],[†] J. M. Gambetta,[2] and A. Blais[1]

[1]*Département de Physique, Université de Sherbrooke, Sherbrooke, Québec J1K 2R1, Canada*
[2]*IBM T. J. Watson Research Center, Yorktown Heights, New York 10598, USA*

We study bifurcation measurement of a multilevel superconducting qubit using a nonlinear resonator biased in the straddling regime, where the resonator frequency sits between two qubit transition frequencies. We find that high-fidelity bifurcation measurements are possible because of the enhanced qubit-state-dependent pull of the resonator frequency, the behavior of qubit-induced nonlinearities, and the reduced Purcell decay rate of the qubit that can be realized in this regime. Numerical simulations find up to a threefold improvement in qubit readout fidelity when operating in, rather than outside of, the straddling regime. High-fidelity measurements can be obtained at much smaller qubit-resonator couplings than current typical experimental realizations, reducing spectral crowding and potentially simplifying the implementation of multiqubit devices.

I. INTRODUCTION

Circuit quantum electrodynamics (cQED), where super-conducting qubits are coupled to transmission-line resonators, constitute a promising architecture for the realization of a quantum information processor [1,2]. Two criteria required for quantum computation are the implementation, in a scalable way, of a universal set of gates and the ability to faithfully measure the qubit state [3]. In this system, single-qubit gates can be performed by sending microwave signals through the resonator close to the qubits' transition frequency, while two-qubit gates can be performed by tuning the qubits in and out of resonance. The increasing fidelity of one-qubit [4] and two-qubit [5–7] gates has allowed cQED to reach important milestones, such as the implementation of two- and three-qubit quantum algorithms [8–10] and the realization of more complex multiqubit devices [11].

Qubit measurement in cQED is realized by driving the resonator close to its natural resonance frequency and by measuring the reflected or transmitted microwave signal. Recently, high-fidelity single-shot measurements have been achieved by using very large measurement drive powers [12–14], by turning the resonator into a nonlinear active device and using bifurcation to distinguish the qubit states [15–17], or by using nearly quantum-limited amplifiers [18]. In these realizations, increasing the qubit-resonator coupling leads to larger variation of the resonator's parameters with the qubit state, resulting in a high measurement fidelity. In the same way, increasing this coupling also typically reduces the gate time of two-qubit operations. However, stronger coupling can also reduce the on/off ratio of logical gates, causes spectral crowding, and reduces the qubit lifetime through spontaneous emission via the resonator, also known as the Purcell effect.

In this paper, we take a different approach and show that it is possible to implement high-fidelity single-shot measurements of a superconducting qubit using relatively small qubit-

resonator coupling strengths—of the order of 10 MHz—than in many recent experiments. To achieve this, we use the weakly anharmonic multilevel structure relevant for most superconducting qubits and take advantage of the so-called straddling regime where the resonator frequency sits between two qubit transitions [19]. This regime shows enhanced qubit-state-dependent pull of the resonator frequency, enhanced qubit-induced resonators, and a reduced Purcell decay rate. We show that these three characteristics combine to improve bifurcation measurements of the qubit state. In numerical simulations of qubit readout, we find error probabilities three times smaller inside with respect to outside of the straddling regime. Even without thorough exploration of the available parameter space, we find measurement fidelities of 98%.

The paper is organized as follows. In Sec. II, we first introduce the Hamiltonians modeling a nonlinear resonator, required for bifurcating measurements, coupled to a multilevel qubit. Then, in Sec. III, we review the principle of bifurcation measurements and highlight the important differences between two-level and multilevel qubits in this respect. In Sec. IV, we derive an effective dispersive Hamiltonian valid in the straddling regime. Finally, in Sec. V we compare the parameters calculated with our model to the parameters extracted from exact diagonalization of the qubit-resonator Hamiltonian. We then examine the specifics of bifurcation in the straddling regime, extract measurement fidelities from numerical simulations, and discuss other advantages of working in this regime.

II. MODEL

As mentioned above, many superconducting qubits have a relatively small anharmonicity and are therefore described by M-level systems with $M > 2$ rather than by two-level systems [19–22]. We consider such a qubit coupled to a Kerr nonlinear resonator (KNR), which could be realized, for example, by an LC circuit with a Josephson junction [15] or a stripline resonator with one [17] or many [23,24] embedded Josephson junctions making it nonlinear. The qubit-resonator system can be modeled with the many-level version of the Jaynes-Cummings Hamiltonian,

$$H_s = H_q + H_r + H_I, \tag{2.1}$$

————
[*]maxime.boissonneault@usherbrooke.ca
[†]Present address: Calcul Numérique et Scientifique à l'Université Laval (CoNSUL) and Calcul Québec, Université Laval, Québec, Québec G1V 0A6, Canada.

where ($\hbar = 1$)

$$H_q = \sum_{i=0}^{M-1} \omega_i \Pi_{i,i} \equiv \Pi_\omega \qquad (2.2)$$

is the qubit Hamiltonian,

$$H_r = \omega_r a^\dagger a + \frac{K}{2} a^\dagger a^\dagger a a \qquad (2.3)$$

is the nonlinear resonator Hamiltonian [25], and

$$H_I = \sum_{i=0}^{M-2} g_i (a^\dagger \Pi_{i,i+1} + a \Pi_{i+1,i}) \qquad (2.4)$$

is the interaction Hamiltonian and where $\Pi_{i,j} \equiv |i\rangle \langle j|$, with $\{|i\rangle\}$ the qubit eigenstates. In these expressions, ω_i is the frequency associated with the qubit eigenstate $|i\rangle$, ω_r is the bare resonator frequency (at low powers), K is the Kerr constant, and g_i are the qubit-resonator coupling constants. We have also introduced the short-hand notation

$$\Pi_x \equiv \sum_{i=0}^{M-1} x_i \Pi_{i,i}, \qquad (2.5)$$

where x is a scalar taking different values x_i associated with the different qubit states $|i\rangle$. This notation is used throughout this paper. Finally, in the qubit-resonator interaction term, we have made the standard rotating-wave approximation and also assumed that transition between states $|i\rangle \leftrightarrow |j\rangle$ is suppressed for $|i - j| \neq 1$ [19].

Measurement of the qubit is realized by driving the resonator with a tone of amplitude ϵ_d and frequency ω_d. This is modeled by the drive Hamiltonian

$$H_d = \epsilon_d (e^{-i\omega_d t} a^\dagger + e^{i\omega_d t} a), \qquad (2.6)$$

leading to the total Hamiltonian

$$H = H_s + H_d. \qquad (2.7)$$

Typical parameters for this system are in the gigahertz range for the qubit and resonator transition frequencies. Couplings g_i can range from 0 up to many hundreds of megahertz in the ultrastrong regime [26–28]. Finally, the nonlinearity K can range from 0 up to many hundreds of megahertz [29], at which point the nonlinear resonator essentially behaves as a qubit. In this paper, we are interested in a regime where the couplings g_i are below a few hundreds of megahertz and the nonlinearity K is limited to, at most, a few megahertz.

III. BASICS OF BIFURCATION MEASUREMENTS

The description of the KNR is simplified by introducing the reduced detuning frequency $\Omega \equiv 2(\omega_r - \omega_d)/\kappa$ [30]. As illustrated in Fig. 1, the steady-state response of the KNR can vary drastically whether the reduced detuning Ω is larger or smaller (in absolute value) than a critical detuning $\Omega_C = \sqrt{3}$. For $|\Omega/\Omega_C| < 1$, the resonator response is single valued, with, as shown in Fig. 1(a), a response that is stiffened compared to the usual Lorentzian line shape. Close to, but below, the critical point, the resonator can then be used as a parametric amplifier for small signals [23]. On the other hand, for $|\Omega/\Omega_C| > 1$ the resonator is in the so-called bifurcation amplification (BA)
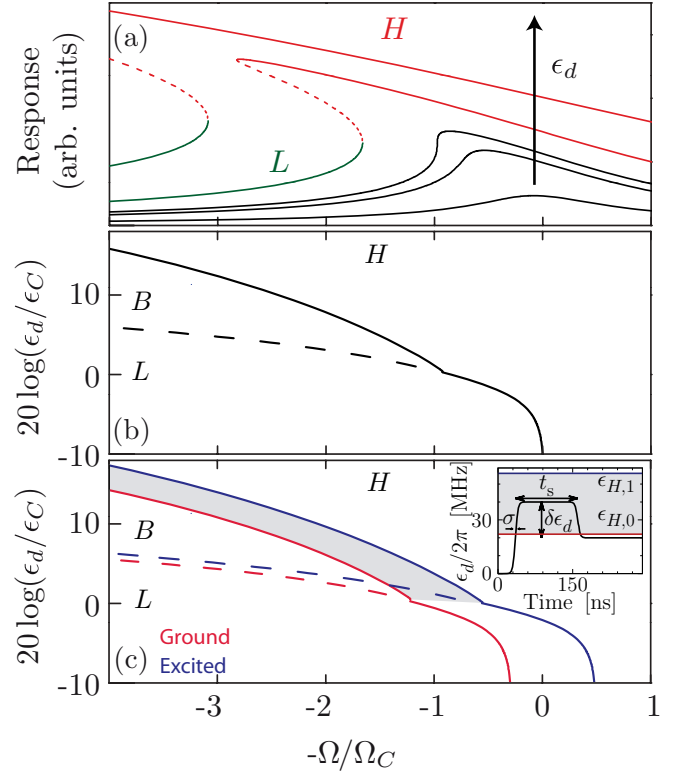

FIG. 1. (Color online) (a) Response (amplitude of the field) as a function of the reduced detuning and for increasing drive amplitude ϵ_d. The back-bending of the response reflects the choice $K < 0$, as is usually the case in circuit QED. (b), (c), Stability diagram of a Kerr nonlinear resonator in the absence (b) or presence (c) of a qubit. Inset: Time-dependent envelope of a sample-and-hold readout. This figure is presented for illustrative purposes, with typical, but unimportant parameter values.

regime, where it is bistable for a range of drive amplitudes ϵ_d. If ϵ_d is ramped up starting from 0, the resonator's response will bifurcate from a low (L) to a high (H) oscillation amplitude dynamical state at a critical amplitude ϵ_H. If the drive amplitude is then reduced, the resonator stays in state H until the drive amplitude becomes lower than a second threshold, ϵ_L. The associated stability diagram is illustrated in Fig. 1(b).

As already experimentally demonstrated, in the BA regime, the KNR can be used as a sample-and-hold detector of a qubit [16,17,31,32]. Indeed, as for most quantum-information-related tasks, qubit readout is realized in the dispersive regime where $|g_i| \ll |\omega_r - \omega_{i+1,i}|$. In this situation, the system Hamiltonian H_s is well approximated by the effective Hamiltonian [33]

$$H_D \approx (\omega_r + \Pi_S) a^\dagger a + \frac{K}{2} a^\dagger a^\dagger a a + \Pi_\omega. \qquad (3.1)$$

As can be seen from the coefficient of $a^\dagger a$, in this regime, the presence of the qubit results in a shift of the resonator frequency by a qubit-state-dependent quantity S_i. This dispersive cavity pull, whose value S_i is discussed below, results in different thresholds $\epsilon_{L,i}$ and $\epsilon_{H,i}$ depending on the qubit states. This is schematized for the first two qubit states $\{|0\rangle, |1\rangle\}$ by the red and blue lines in Fig. 1(c).

Starting from 0, increasing the drive amplitude ϵ_d until $\epsilon_{H,0} < \epsilon_d < \epsilon_{H,1}$ will result in a high amplitude of the cavity field if the qubit is in its ground state and a low amplitude if it is in its excited state. This range is represented by the shaded (gray) area in Fig. 1(c). If the drive amplitude is then reduced below $\epsilon_{H,0}$, but stays above $\epsilon_{L,1/0}$ [see inset in Fig. 1(c)], both resulting states are stable and the qubit state has been mapped into the dynamical state of the resonator. Since these dynamical states are stable, it is possible to accumulate the output signal for a time longer than the qubit relaxation time T_1. The measurement fidelity can then be optimized by varying the sampling time t_s, the height of the plateau $\delta\epsilon_m$, and the steepness of the ramp up σ [16,17,31,32].

In practice, the readout fidelity is limited by qubit relaxation during or before the sample phase [17], when the resonator has not bifurcated yet. The speed at which the sampling can be made is limited by the resonator's decay rate κ. Indeed, ramping up the drive much faster than $1/\kappa$ will produce large ringing oscillations in the field amplitude, which can result in false positives or negatives. This results in a reduced measurement fidelity. Increasing κ therefore implies smaller transients and hence faster measurement. However, increasing κ too much can also yield a lower measurement fidelity. Indeed, in the limit where κ is much larger than the difference between the qubit-state-dependent resonator pulls $\chi \equiv S_1 - S_0$, both qubit states are indistinguishable. Moreover, increasing κ also increases the qubit's Purcell decay rate $\gamma_\kappa \sim \kappa g_i^2/(\omega_{i+1} - \omega_i - \omega_r)^2$ [34,35], which ultimately limits the qubit relaxation time T_1. Ideally, one would like to increase both χ and κ, without increasing the Purcell rate.

A. Two-level systems

The qubit-state-dependent resonator shift S_i discussed above depends on the coupling g_i and the qubit-resonator detuning $\Delta_{i,r} \equiv \omega_{i+1} - \omega_i - \omega_r$. For a two-level qubit, it takes the simple form [1]

$$S_{1/0}^{2LS} = \pm\frac{g_0^2}{\Delta_{0,r}}, \tag{3.2}$$

corresponding to symmetric displacement of the cavity frequency around its bare frequency ω_r. The difference between the pulled resonator frequency for qubit states $|0\rangle$ and $|1\rangle$ is therefore $\chi = S_1 - S_0 = 2g_0^2/\Delta_{0,r}$. This cavity pull can be of the order of a few tens of megahertz, while staying in the dispersive regime, with typical values $g_0/2\pi \sim 100$–200 MHz and $\Delta_{0,r}/2\pi \sim 1$–2 GHz. Such couplings have been achieved with transmons and flux qubits [36,37]. For a two-level qubit, increasing the coupling g_0 increases χ, but also increases γ_κ by the same amount. For Purcell-limited qubits, this negates the gain of this strategy.

B. Multilevel systems

For multilevel systems, the shifts are changed by the presence of additional levels, and the symmetry around the bare resonator frequency is broken. Indeed, the frequency shift is given by Ref. [19]

$$S_i^{MLS} = \frac{g_{i-1}^2}{\Delta_{i-1,r}} - \frac{g_i^2}{\Delta_{i,r}}. \tag{3.3}$$
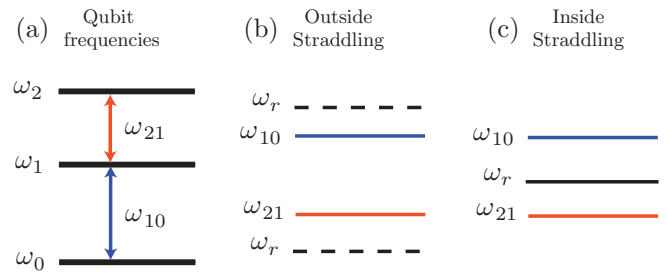

FIG. 2. (Color online) (a) Absolute and transition frequencies of the first three eigenstates of a qubit with negative anharmonicity such as the transmon. (b) Example of a frequency diagram where the resonator frequency (dashed lines) is outside of a straddling regime. (c) Example of an energy diagram where the resonator frequency [middle solid (black) line] is inside of a straddling regime. Typical transition frequencies (ω_{10}, ω_{21}) are in the gigahertz range, with anharmonicity in the few hundreds of megahertz range.

As illustrated in Fig. 2(b), in most experiments [8,17,30] the qubits are biased such that the resonator frequency sits above, or below, all of the qubit transition frequencies. This results in a pull of the resonator frequency $\chi = 2g_0^2/\Delta_{0,r} - g_1^2/\Delta_{1,r}$, reduced compared to that of a purely two-level system. In the limit where the multilevel system tends toward an harmonic oscillator, $\Delta_{1,r} \to \Delta_{0,r}$ and $g_1 \to \sqrt{2}g_0$ such that this pull vanishes. The reduction in the pull can be compensated with larger couplings g_i, achieved, for example, with transmons [20]. However, as stated above, increasing the qubit-resonator coupling also increases the resonator-mediated Purcell decay [35] and dressed dephasing [38–40]. This dependence on κ and g_i of both resonator-mediated qubit decay and measurement speed ultimately limits the achievable measurement fidelity.

One way to increase the dispersive shifts χ without increasing the coupling is to work in the so-called straddling regime [19]. In this regime, illustrated in Fig. 2(c), the detunings $\Delta_{1,r}$ and $\Delta_{0,r}$ are of opposite signs. As a result, instead of canceling each other, the two terms in Eq. (3.3) add up, yielding a significantly enhanced value of χ. Since this improvement is obtained without increasing g_i, it does not increase the Purcell rate. Moreover, as we show in the next section, this regime also increases qubit-induced nonlinearities [13], something that we exploit below to improve bifurcation readouts.

IV. DISPERSIVE MODEL IN THE STRADDLING REGIME

Following the approach of Ref. [33], we use a polaron transformation [41–43] followed by a dispersive transformation [38,44] to approximately diagonalize the Hamiltonian of Eq. (2.7). Doing the transformations in this order (polaron followed by dispersive) allows us to correctly model the ac-Stark shift caused by a drive detuned from the resonator frequency [33]. However, since we are interested in the straddling regime, one more transformation must be done in order to diagonalize an effective two-photon process that is important only in the straddling regime. This is done in the Appendix and yields the effective diagonal Hamiltonian

$$H' = \Pi_{\omega'} + [\omega_r'(\alpha) + \Pi_{S(\alpha)}]a^\dagger a, \tag{4.1}$$

where $\omega_r'(\bar{\alpha})$ is the Kerr-shifted resonator frequency

$$\omega_r'(\alpha) \equiv \omega_r + 2K|\bar{\alpha}|^2, \qquad (4.2)$$

with $\bar{\alpha} \equiv \langle \Pi_\alpha \rangle$ the resonator mean field, and

$$\omega_i' = \omega_i + \mathbb{S}_i|\bar{\alpha}|^2 + \mathbb{K}_i|\bar{\alpha}|^4 + L_i(\bar{\alpha}) \qquad (4.3)$$

are the renormalized effective qubit frequencies. There, we have defined

$$\mathbb{S}_i \equiv -(X_i - X_{i-1}), \qquad (4.4a)$$

$$\begin{aligned}
\mathbb{K}_i \equiv & -\mathbb{S}_i(|\Lambda_i|^2 + |\Lambda_{i-1}|^2) \\
& - \tfrac{1}{4}(3X_{i+1}|\Lambda_i|^2 - X_i|\Lambda_{i+1}|^2) \\
& + \tfrac{1}{4}(3X_{i-2}|\Lambda_{i-1}|^2 - X_{i-1}|\Lambda_{i-2}|^2) \\
& - X_i^{(2)} + X_{i-2}^{(2)}, \qquad (4.4b)
\end{aligned}$$

the linear and quadratic ac-Stark shift coefficients with $\Lambda_i \equiv -g_i/\Delta_{i,d}$ and $X_i \equiv -g_i\Lambda_i$ and where $\Delta_{i,d} \equiv \omega_{i+1} - \omega_i - \omega_d$ is the detuning between the qubit transition i and the drive d. The last line of $\mathbb{K}_i$ comes from the diagonalization of an effective two-photon transition process that is large only in the straddling regime. This contributes the last two terms of $\mathbb{K}_i$ with $X_i^{(2)} = -g_i^{(2)}\Lambda_i^{(2)}$, $\Lambda_i^{(2)} = -g_i^{(2)}/(\Delta_{i+1,d} + \Delta_{i,d})$, and where

$$g_i^{(2)} = \Lambda_i\Lambda_{i+1}(\Delta_{i+1,d} - \Delta_{i,d}). \qquad (4.5)$$

We note that, compared with the results of Ref. [13], the detunings Δ_i are defined with respect to the *drive* frequency, and not the *resonator* frequency. In addition, in Ref. [13], the dispersive transformation was done with respect to the field operator a rather than to the classical field α. Because of this choice, the quadratic term $\mathbb{S}_i$ in Ref. [13] contains a correction which accounts for a specific choice of ordering for the ladder operators in the quartic term. Here, since it is the classical field that is considered, there are no such corrections (i.e., $\alpha\alpha^* = \alpha^*\alpha$).

Finally, in Eq. (4.3) we have also defined the Lamb shift

$$L_i(\alpha) = \frac{g_i^2}{\omega_{i+1}''(\alpha) - \omega_i''(\alpha) - \omega_r'(\alpha)}, \qquad (4.6)$$

where ω_i'' is given by

$$\omega_i'' = \omega_i + \mathbb{S}_i|\bar{\alpha}|^2 + \mathbb{K}_i^{(1)}|\bar{\alpha}|^4. \qquad (4.7)$$

Using this definition, the cavity pull $\Pi_{S(\alpha)}$ in the effective Hamiltonian, Eq. (4.1) can be expressed in a compact way using $S_i(\alpha) = -[L_{i+1}(\alpha) - L_i(\alpha)]$. We note that while the ac-Stark shift coefficients $\mathbb{S}_i$ and $\mathbb{K}_i$ depend on the qubit-drive detuning, the Lamb shift L_i depends on the detuning between the ac-Stark shifted qubit and the Kerr-shifted resonator [33]. Finally, the steady-state qubit-state-dependent cavity field α_i is given by the solution of

$$-\epsilon_d = \left(\omega_r - \omega_d - i\frac{\kappa}{2}\right)\alpha_i + K|\alpha_i|^2\alpha_i + \left(\mathbb{S}_i + \frac{4}{3!}\mathbb{K}_i|\alpha_i|^2\right)\alpha_i. \qquad (4.8)$$

In Fig. 3, we compare the above analytical expressions for $\mathbb{S}_i$ and $\mathbb{K}_i$ to numerical results. These quantities are found numerically by fitting a quadratic polynomial to the resonator frequency for the qubit state $|i\rangle$ and in the presence of n
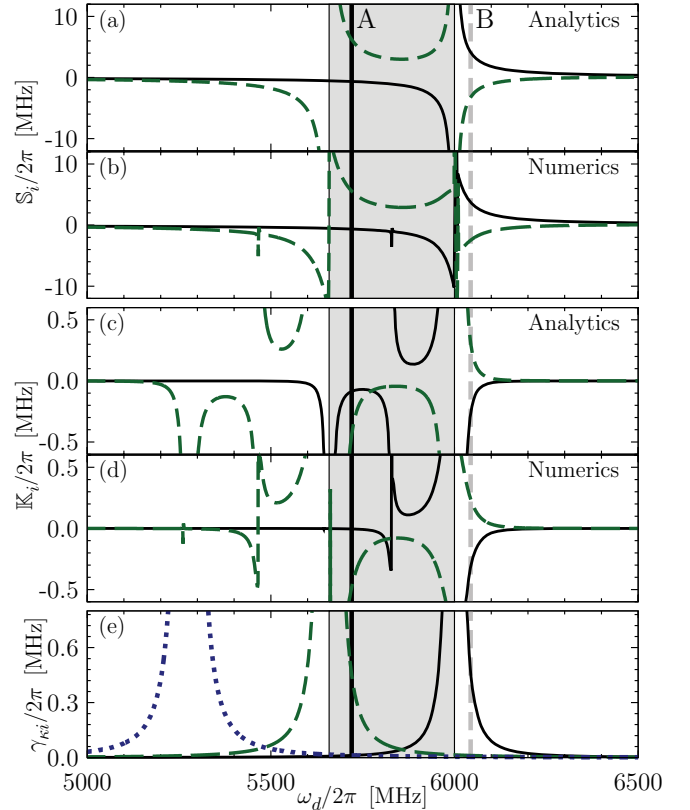

FIG. 3. (Color online) (a), (b), Linear and (c), (d), quadratic ac-Stark shifts for the ground [solid (black) lines] and the excited [dashed (green) lines] states of a transmon qubit [19] with charging energy $E_C = 300$ MHz, Josephson energy $E_J = 25$ GHz, and coupling at zero flux $g_{10}/2\pi = 15$ MHz tuned such that $\omega_{10}/2\pi = 6$ GHz. This yields $(\omega_0, \omega_1, \omega_2, \omega_3)/2\pi \approx (0, 6, 11.7, 16.9, 21.8)$ GHz and $(g_{10}, g_{21}, g_{32}, g_{43})/2\pi = (13.5, 18.5, 21.8, 24.1)$ MHz at the operating point. (a) and (c) correspond to the analytical equations, Eq. (4.4), while (b) and (d) are extracted numerically as described in the text. (e) Purcell decay rate $\gamma_{\kappa i} = \kappa g_i^2/\Delta_{i,r}^2$ assuming $\kappa/2\pi = 5$ MHz and $\omega_r = \omega_d$ for $i = 0$ [solid (black) line], $i = 1$ [dashed (green) line] and $i = 2$ [dotted (blue) line]. The solid (black) line, corresponding to the $|1\rangle \rightarrow |0\rangle$ transition, is the relevant one for qubit operation. The shaded area corresponds to the straddling regime. The solid vertical (black) line and the dashed vertical (gray) line correspond to the two operating points A $(\omega_d/2\pi = 5720$ MHz) and B $(\omega_d/2\pi = 6044$ MHz) discussed in Secs. IV and V.

photons, $\omega_{r,i}(n) = E_{i,n+1} - E_{i,n}$. The energy $E_{i,n}$ is found numerically by diagonalizing the undriven qubit-resonator Hamiltonian H_s and taking $K = 0$. We then associate $E_{i,n}$ with the energy of the eigenstate closest to the bare qubit-resonator state $|i,n\rangle$. The parameters, given in the caption to Fig. 3, are typical to transmon qubits [19] but with a smaller than typical coupling, $g_{10}/2\pi = 13.5$ MHz. We show the analytical [Figs. 3(a) and 3(c)] and numerical [Figs. 3(b) and 3(d)] values of $\mathbb{S}_i$ [Figs. 3(a) and 3(b)] and $\mathbb{K}_i$ [Figs. 3(c) and 3(d)] for the ground state $i = 0$ [solid (black) lines] and first qubit excited states $i = 1$ [dashed (green) lines]. We find quantitative agreement, except at the qubit-resonator resonances and at the two-photon resonances (identified by divergences). We finally

show in Fig. 3(e) the Purcell decay rate $\gamma_{\kappa i}$ of level i assuming $\omega_r = \omega_d$ and $\kappa/2\pi = 5$ MHz.

Two operating points, designated A and B and identified by the solid vertical (black) lines and vertical dashed (gray) lines, respectively, are illustrated in Fig. 3. These particular points have been chosen because, while A lies in the straddling regime and B is outside of that regime, the cavity pull $|\chi| = |\mathbb{S}_1 - \mathbb{S}_0|$ is identical in both cases. In the next section, we show that working in the straddling regime is advantageous for qubit readout. Since the cavity pull is the same at both A and B, improvement in the measurement will be due to qubit-induced nonlinearities $\mathbb{K}_i$ or variation in the Purcell decay rate.

The qubit-induced nonlinearities $\mathbb{K}_i$ are plotted in Figs. 3(c) and 3(d). Comparing Figs. 3(a) and 3(c), we note a major difference between the operating points A and B. At B, the sign of $\mathbb{K}_i$ is opposite to that of $\mathbb{S}_i$ for both $i = 0$ [solid (black) lines] and $i = 1$ [dashed (green) lines]. This sign difference corresponds to a cavity pull that is *decreasing* when the number of photons increases. On the other hand, at point A, the sign of $\mathbb{K}_0$ is the same as that of $\mathbb{S}_0$. Therefore, we expect that the cavity pull at point A will not decrease as much as at point B with increasing photon number [13]. Moreover, we can see in Fig. 3(e) that the Purcell rate for the transition $|1\rangle \rightarrow |0\rangle$ [solid (black) line] is much larger at point B than at point A.

One would expect that these two effects—a cavity pull that reduces less with an increasing number of photon and a reduced Purcell decay rate—lead to better qubit measurement at operating point A than at B. In the next section, we show numerically that this expectation holds for a Kerr resonator operated close to its bifurcation point. This is done by first calculating the steady-state photon number associated with both qubit states. We then simulate the complete dynamics corresponding to a qubit under measurement with the microwave pulse typically used in bifurcating readouts [17,31,45] and which is designed to make the resonator latch in its H state for one of the qubit state. From these simulations, we extract the expected measurement fidelity and show that better results are indeed obtained at operating point A than at B.

V. IMPROVING BIFURCATION MEASUREMENTS IN THE STRADDLING REGIME

Bifurcation measurements rely on the critical drive amplitude $\epsilon_{H,i}$—at which the resonator bifurcate to its high state H—being different for each qubit state i. As illustrated in the inset in Fig. 1(c), in bifurcation measurements the measurement drive amplitude ϵ_d is increased to a value between these two critical amplitudes. However, the bifurcation process being probabilistic, the resonator can still bifurcate from the L to the H state even if the drive amplitude is (slightly) lower than ϵ_H. This yields errors in the measurement and a reduced measurement fidelity. We therefore expect the measurement fidelity to increase with $\Delta\epsilon_H \equiv |\epsilon_{H,0} - \epsilon_{H,1}|$ and so, in other words, with cavity pull. In addition, one expects that a larger separation of the thresholds protects the measurement better against ringing in the resonator's response, which, close to ϵ_H, may lead to unwanted bifurcation. For these reasons, we expect that operating point A, at which the cavity pull should remain larger on a wider range of measurement power, to be better for measurement than point B.
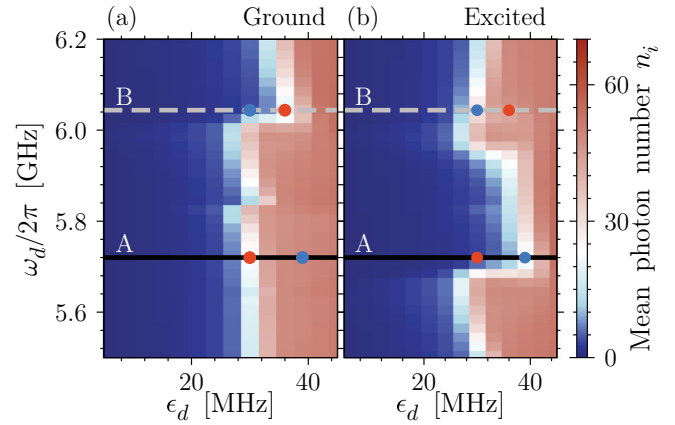

FIG. 4. (Color online) Numerically computed average number of photons n_i for a qubit initialized in state $|i\rangle$ with (a) $i = 0$ and (b) $i = 1$ without qubit relaxation or dephasing. The evolution is computed according to Eq. (5.1). Qubit parameters are given in the caption to Fig. 3. Resonator parameters are $(\kappa, K)/2\pi = (5, -0.4)$ MHz and the resonator frequency is adjusted to keep the resonator-drive detuning $(\omega_r - \omega_d)/2\pi = 15$ MHz such that the reduced detuning $\Omega/\Omega_C \sim 3.5$, well in the bifurcation regime. Dashed lines represent the two operating points A and B (see caption to Fig. 3). Filled circles indicate the bifurcation thresholds $\epsilon_{H,i}$ (red for $i = 0$, blue for $i = 1$).

Below, we first calculate the steady-state response of the resonator in Sec. V A. We then compute the measurement fidelity for a pulsed measurement in Sec. V B. Finally, we discuss other advantages of working in the straddling regime in Sec. V C.

A. Steady-state response

We simulate the evolution of the state ρ starting with the resonator in the vacuum and with the qubit either in the eigenstate $|0\rangle$ or $|1\rangle$. We first focus on a drive of constant amplitude ϵ_d, without intrinsic qubit relaxation or dephasing. By looking at the resonator's steady-state response, with this simulation, we want to show that the distance between the bifurcation thresholds $\epsilon_{H,0}$ and $\epsilon_{H,1}$ is indeed larger at operating point A than at B. The evolution is governed by the master equation

$$\dot{\rho} = -i[H, \rho] + \kappa \mathcal{D}[a]\rho, \qquad (5.1)$$

with the Linblad-form dissipator $\mathcal{D}[a] = \frac{1}{2}(2a\rho a^\dagger - a^\dagger a\rho - \rho a^\dagger a)$. After a time long compared with $1/\kappa$, we compute the average number of photons n_i for the qubit initially in state $i \in \{0,1\}$.

This quantity is plotted in Fig. 4 as a function of the drive frequency ω_d and amplitude ϵ_d for the qubit initially in its ground [Fig. 4(a)] or excited [Fig. 4(b)] state. In both cases, two regions, corresponding, respectively, to the resonator being in the L state (dark blue; $n_i < 10$ photons) or in the H state (light red; $n_i \sim 50$ photons), can be identified. The border between these two regions (white) corresponds to the critical drive amplitude $\epsilon_{H,i}$, at which the photon population goes sharply from $n_i \sim 15$ to $n_i \sim 50$. Comparing these results to the dispersive shifts illustrated in Fig. 3, we can see that sharp changes in $\mathbb{S}_i$ and $\mathbb{K}_i$ translate into sharp changes in the bifurcation amplitudes $\epsilon_{H,i}$. For example, both $\mathbb{S}_0$ and $\mathbb{S}_1$

[Fig. 3(a)] change sign at $\omega_d/2\pi = 6$ GHz, which translates to a sharp change in both $\epsilon_{H,i}$ around that frequency. Moreover, $\mathbb{S}_1$ changes sign at $\omega_d/2\pi \approx 5.7$ GHz, while $\mathbb{S}_1$ does not. As a result, as shown in Fig. 4, only $\epsilon_{H,1}$ changes significantly at that frequency. Finally, variations in $\mathbb{K}_i$ are also visible, for example, as the feature in $\epsilon_{H,0}$ at $\omega_d/2\pi \approx 5.85$ GHz, corresponding to the change of sign in $\mathbb{K}_0$ at that same frequency.

Operating points A and B are illustrated in Fig. 4 by the solid horizontal (black) lines and dashed horizontal (gray) lines, respectively. The thresholds $\epsilon_{H,i}$ at these two points are identified by filled circles (red for $\epsilon_{H,0}$ and blue for $\epsilon_{H,1}$). As expected from the above arguments, the separation $\Delta\epsilon_H \equiv |\epsilon_{H,0} - \epsilon_{H,1}|$ is larger at A than at B. For the chosen parameters, we find $\Delta\epsilon_H/2\pi \sim 10$ MHz at A, while we find $\Delta\epsilon_H/2\pi \sim 5$ MHz at B. We note that $\epsilon_{H,1} > \epsilon_{H,0}$ at point A, while $\epsilon_{H,1} < \epsilon_{H,0}$ at point B. This simply changes which resonator state—of L and H—is associated with each qubit state.

B. Pulsed measurement fidelity

In order to quantify by how much an actual measurement can be improved by working at operating point A—inside the straddling regime—rather than at point B—outside of the straddling regime—we numerically simulated a bifurcation measurement with a sample-and-hold-shaped pulse as illustrated in the inset in Fig. 1(c). We recall that, to our knowledge, all experiments with bifurcation measurements have been made outside of the straddling regime so far.

To be more realistic, we performed numerical integration of the master equation, Eq. (5.1) including qubit dissipation modeled using the Lindblad-form term $\gamma \sum_{i=0}^{M-2} \mathcal{D}[\frac{g_i}{g_0}\Pi_{i,i+1}]\rho$. Here, γ is the decay rate of the first qubit transition and the factor g_i/g_0 is included to take into account the variation of the qubit decay rate with increasing i [33]. Pure dephasing is not included since recent devices tend to have very low pure dephasing rates [20,21]. Including this effect would possibly affect the QND character of the readout due to dressed dephasing [38–40], but the extent of this effect has yet to be measured experimentally.

At the end of the hold time, the Q function of the resonator $Q(\alpha) = \langle\alpha|\rho|\alpha\rangle/\pi$ is computed. A typical Q function near the bifurcation threshold ϵ_H is represented in Fig. 5. It shows
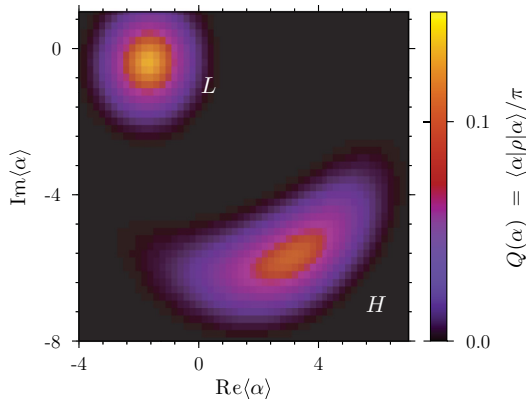

FIG. 5. (Color online) Typical Q function $Q(\alpha)$ of a resonator when driven close to its bifurcation threshold ϵ_H.
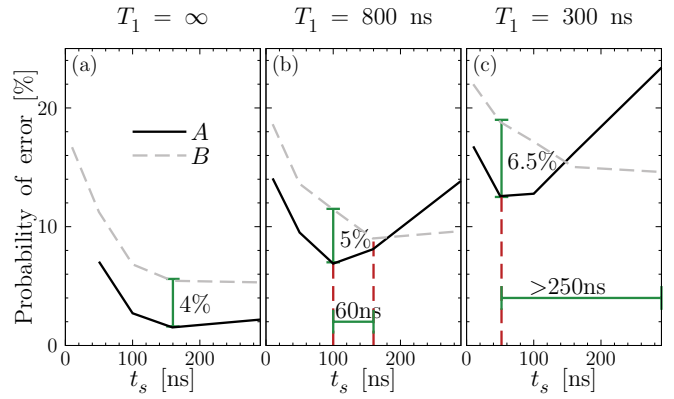

FIG. 6. (Color online) Error probability for the outcome of a bifurcation measurement versus sampling time t_s. The measurement pulsed is illustrated in the inset in Fig. 1(c). Solid (black) lines correspond to operating point A, in the straddling regime, and dashed (gray) lines correspond to operating point B, outside of the straddling regime. Parameters are the same as in Fig. 4. Simulations are realized for a qubit with intrinsic relaxation times (a) $T_1 = \infty$, (b) $T_1 = 800$ ns, and (c) $T_1 = 300$ ns. (b), (c), Vertical dashed (red) lines indicate the minimum of the curves for the two operating points. Solid (green) bars indicate the gain in measurement time (horizontal) or measurement fidelity (vertical) between the two operating points.

two well-separated smooth peaks corresponding to the L and H states of the resonator. The switching probability is extracted from the weight of the peak that is the farthest away from the origin. From the switching probabilities, the worst-case error probability,

$$P_{\text{error}} = \max_{\substack{\{i,j\} \in \{0,1\} \\ j \neq i}} P(j|i), \qquad (5.2)$$

can be computed, where $P(j|i)$ is the probability of assigning the measurement to the qubit state $|j\rangle$, given that the qubit was initially in $|i\rangle$. This numerical procedure was previously tested against experimental single-shot bifurcation measurement of a transmon qubit [17] and an identical measurement fidelity was found, within a margin of 2% [46].

We show in Fig. 6 the worst-case error probability as a function of the sampling time t_s for three qubit relaxation times T_1. These results have been obtained by minimizing the error probability with respect to σ and $\delta\epsilon_d$ [see inset in Fig. 1(c) for definitions]. Comparing Figs. 6(a)–6(c), we see that the P_{error} increases as the qubit relaxation time decreases, which is expected because of the increased odds of the qubit relaxing before the resonator switches from L to H.

We now compare the results inside [solid (black) lines; operating point A] and outside [dashed (gray) lines; operating point B] of the straddling regime. We first observe that for short sampling times t_s, the error probability is always lower for operating point A than B. Since the low-photon cavity pulls χ were chosen to be the same for both points, this improvement is due to both the sign and the amplitude of the Kerr terms $\mathbb{K}_i$ and to the reduced Purcell decay as explained in Sec. IV. The situation is, however, reversed for larger t_s where point B is superior. As illustrated in Fig. 4, this is because the resonator switches at a lower power for the ground state than for the excited state at point A, while the opposite is true for point B.

This implies that qubit relaxation induces resonator switching (i.e., false positives) at point A but not at point B. We note that the situation would be reversed for a qubit with a positive anharmonicity such as the low-impedance flux qubit [22], increasing further the advantage of working in the straddling regime.

Overall, we find that operating within the straddling regime always allows us to reach lower error probabilities with a sampling time t_s always as short as, or shorter than, outside of the straddling regime. When operating in the straddling regime, the error probability is up to 3 times lower than outside. Finally, the absolute improvement is better for qubits with shorter lifetimes, but as expected, the best fidelity is found for qubits with longer lifetimes.

C. Other advantages

The above improvement in readout fidelity has been obtained by working with a qubit-resonator coupling g that is more than an order of magnitude smaller than current experimental realizations. Lower coupling, however, leads to slower two-qubit gates when these rely on qubit-qubit interactions mediated by the same resonator mode that is used for readout. This problem can be sidestepped by either taking advantage of different modes for readout and two-qubit gates [47] or, as recently experimentally realized, using direct capacitive coupling between the qubits [48,49].

With the above problem avoided, working with weaker coupling g can be advantageous in other ways than the more efficient readout studied here. For example, it allows us to greatly reduce the Purcell decay by biasing the qubit away from a resonator resonance when it is not being measured. With a reduction in the coupling by a factor of 10, a reduction in the Purcell decay rate by a factor of 100 can be obtained for the same detuning and cavity damping [see solid (black) line in Fig. 3(e)]. At the time of measurement, the qubit-resonator detuning can be adjusted so as to reach the straddling regime. This can be done by changing the flux in the qubit loop or by using a tunable resonator (or both) [50]. Moving in and out of the straddling regime in this way necessarily means going through a qubit-resonator crossing. With a large coupling g, the associated (and unwanted) Landau-Zener-Stueckelberg transitions can be correspondingly large [51]. This probability is greatly reduced, however, when working with small couplings. Indeed, assuming a frequency-tuning speed of $v = 2\pi \cdot 1$ GHz/1 ns, one finds the probability of unwanted transition $P = 1 - e^{-2\pi g_0^2/v} = 0.7\%$ for a coupling $g/2\pi = 13.5$ MHz, while the same probability is $\sim 10\%$ for $g/2\pi = 50$ MHz and $\sim 30\%$ for $g/2\pi = 100$ MHz.

Lower coupling strengths can also help to reduce spectral crowding in the presence of multiple qubits coupled to a single resonator. Indeed, even if the qubit-qubit interaction mediated by virtual excitations of the resonator is not actively used for logical gates, it is always present and can lead to errors. The rate of this interaction can be reduced by increasing the qubit-qubit detuning by an amount that is large with respect to the coupling g. With large g and multiple qubits, the available spectral range (typically from ~ 4 to 15 GHz) is rapidly occupied and only a few qubits can be coupled to the same resonator without having to deal with unwanted two-qubit

gates. Using the straddling regime to increase the measurement fidelity with smaller coupling addresses this problem and does not require advanced circuit designs [11].

VI. CONCLUSION

We have studied the measurement of a multilevel superconducting qubit using bifurcation of a KNR and exploiting the straddling regime. The method is applicable to any qubit with a weakly anharmonic multilevel structure with only nearest-level transitions but could be generalized to more complex structures and couplings. As we have shown, working in the straddling regimes allows larger qubit-state-dependent pulls of the resonator frequency for a given coupling or, equivalently, the same pull for smaller couplings. While outside of the straddling regime, the resonator frequency shift is reduced at higher photon numbers [38], we show that, inside the straddling regime, it is possible to find operating points where this reduction is minimized. We also show that the Purcell decay rate can be much lower for a given cavity pull inside the straddling regime. Combined, these two effects lead to an increased fidelity for bifurcation measurements and we find an error probability up to 3 times smaller inside than outside of the straddling regime for a sampling time that can be more than 250 ns shorter. We find measurement fidelities $1 - P_{\text{error}}$ higher than 98% with a qubit-resonator coupling as small as 13.5 MHz with realistic system parameters.

The method presented in this paper also has the advantage of reducing spectral crowding in multiple-qubit systems. It does that without requiring complex circuits and allows us to effectively remove Purcell decay when the qubits are not being measured.

APPENDIX: DISPERSIVE TRANSFORMATION OF THE TWO-PHOTON TERMS

In this Appendix, we follow Ref. [33] to diagonalize Hamiltonian (2.7) as well as a two-photon transition term that can be large only in the straddling regime. To do so, we first apply a polaron transformation [41–43],

$$\mathbf{P} = \sum_{i=0}^{M-1} \Pi_{i,i} D(\alpha_i), \tag{A1}$$

where $D(\alpha)$ is a displacement transformation [52],

$$D(\alpha) = \exp[\alpha a^\dagger - \alpha^* a], \tag{A2}$$

that displaces the resonator field operator $a \to a + \alpha_i$. The result of the polaron transformation on a is therefore $a \to a + \Pi_\alpha$, where Π_α is defined according to Eq. (2.5). We follow this polaron transformation by a dispersive transformation of

the classical detuned drive on the qubit

$$\mathbf{D}_C = \exp\left[\sum_{i=0}^{M-2} \xi_i^* \Pi_{i,i+1} - \xi_i \Pi_{i+1,i}\right], \qquad (A3)$$

where ξ_i is a classical analog of the operator $\lambda_i a^\dagger$ in the dispersive transformation [38,44]. Applying these two transformations on Hamiltonian (2.7) and choosing α_i according to Eq. (4.8) and

$$\xi_i = \frac{-g_i \alpha_i}{\omega_{i+1,i} - \omega_d} \qquad (A4)$$

yields the Hamiltonian [33]

$$H'' = \sum_{i=0}^{M-1} \omega_i'' \Pi_{i,i} + H_I + \omega_r'(\alpha) a^\dagger a$$
$$+ \sum_{i=0}^{M-3} \alpha_i^* \alpha_{i+1}^* e^{-2i\omega_d t} g_i^{(2)} \Pi_{i,i+2} + \text{h.c.}, \qquad (A5)$$

where the dispersive transformation has been performed to fourth order and $g_i^{(2)}$, given by Eq. (4.5), is an effective coupling due to two-photon transitions. In the above Hamiltonian, we have defined the ac-Stark shifted qubit frequencies

$$\omega_i'' = \omega_i + \mathbb{S}_i |\bar{\alpha}|^2 + \mathbb{K}_i^{(1)} |\bar{\alpha}|^4, \qquad (A6)$$

where $\bar{\alpha} = \langle \Pi_\alpha \rangle$, α_i is given by the solution of Eq. (4.8), $\mathbb{S}_i$ is given by Eq. (4.4a), $\mathbb{K}_i^{(1)}$ is given by the first three lines of

Eq. (4.4b), and the Kerr-shifted resonator frequency

$$\omega_r'(\alpha) \equiv \omega_r + 2K|\bar{\alpha}|^2. \qquad (A7)$$

We note that the second line of H'' is not diagonal. In Ref. [33], this term was dropped, assuming that $g_i^{(2)}$ was small and that $|2\omega_d - \omega_{i+2} + \omega_i|$ was large enough to do a rotating-wave approximation. Here, however, since we are interrested in the straddling regime, the same cannot be done. Indeed, if, for example, the drive frequency is $\omega_d = (\omega_2 - \omega_1)/2 + (\omega_1 - \omega_0)/2$, which falls directly in the middle of a straddling regime, the second line of H'' is resonant and a two-photon transition from $|0\rangle$ to $|1\rangle$ is driven. Moreover, since $\Delta_{i+1,d}$ and $\Delta_{i,d}$ have the same sign, the coupling $g_i^{(2)}$ can be large. We can, however, approximately diagonalize this term using a second transformation of the form

$$\mathbf{D}^{(2)} = \exp\left[\sum_{i=0}^{M-3} \xi_i^{(2)*} \Pi_{i,i+2} - \xi_i^{(2)} \Pi_{i+2,i}\right]. \qquad (A8)$$

Applying this transformation to Eq. (A5) and choosing

$$\xi_i^{(2)} = \frac{-g_i^{(2)} \alpha_i \alpha_{i+1}}{\Delta_{i+1,d} + \Delta_{i,d}} \qquad (A9)$$

yields a correction to the Kerr shift, giving Eq. (4.4b). Applying a final dispersive transformation on H'' in order to diagonalize the quantum interaction H_I yields the diagonalized Hamiltonian, (4.1).

---

[1] A. Blais, R.-S. Huang, A. Wallraff, S. M. Girvin, and R. J. Schoelkopf, Phys. Rev. A **69**, 062320 (2004).

[2] A. Wallraff, D. I. Schuster, A. Blais, L. Frunzio, R.-S. Huang, J. Majer, S. Kumar, S. M. Girvin, and R. J. Schoelkopf, Nature **431**, 162 (2004).

[3] D. P. DiVincenzo, F. Phys. **48**, 771 (2000).

[4] A. Wallraff, D. I. Schuster, A. Blais, L. Frunzio, J. Majer, M. H. Devoret, S. M. Girvin, and R. J. Schoelkopf, Phys. Rev. Lett. **95**, 060501 (2005).

[5] J. Majer, J. M. Chow, J. M. Gambetta, J. Koch, B. R. Johnson, J. A. Schreier, L. Frunzio, D. I. Schuster, A. A. Houck, A. Wallraff, A. Blais, M. H. Devoret, S. M. Girvin, and R. J. Schoelkopf, Nature **449**, 443 (2007).

[6] A. O. Niskanen and Y. Nakamura, Nature **449**, 415 (2007).

[7] J. M. Chow, A. D. Corcoles, J. M. Gambetta, C. Rigetti, B. R. Johnson, J. A. Smolin, J. R. Rozen, G. A. Keefe, M. B. Rothwell, M. B. Ketchen, and M. Steffen, Phys. Rev. Lett. **107**, 080502 (2011).

[8] L. DiCarlo, J. M. Chow, J. M. Gambetta, L. S. Bishop, B. R. Johnson, D. I. Schuster, J. Majer, A. Blais, L. Frunzio, S. M. Girvin, and R. J. Schoelkopf, Nature **460**, 240 (2009).

[9] A. Fedorov, L. Steffen, M. Baur, M. P. da Silva, and A. Wallraff, Nature **481**, 170 (2012).

[10] M. D. Reed, L. DiCarlo, S. E. Nigg, L. Sun, L. Frunzio, S. M. Girvin, and R. J. Schoelkopf, Nature **482**, 382 (2012).

[11] M. Mariantoni, H. Wang, T. Yamamoto, M. Neeley, R. C. Bialczak, Y. Chen, M. Lenander, E. Lucero, A. D. O'Connell, D. Sank, M. Weides, J. Wenner, Y. Yin, J. Zhao, A. N. Korotkov, A. N. Cleland, and J. M. Martinis, Science **334**, 61 (2011).

[12] M. D. Reed, L. DiCarlo, B. R. Johnson, L. Sun, D. I. Schuster, L. Frunzio, and R. J. Schoelkopf, Phys. Rev. Lett. **105**, 173601 (2010).

[13] M. Boissonneault, J. M. Gambetta, and A. Blais, Phys. Rev. Lett. **105**, 100504 (2010).

[14] L. S. Bishop, E. Ginossar, and S. M. Girvin, Phys. Rev. Lett. **105**, 100505 (2010).

[15] I. Siddiqi, R. Vijay, F. Pierre, C. M. Wilson, M. Metcalfe, C. Rigetti, L. Frunzio, and M. H. Devoret, Phys. Rev. Lett. **93**, 207002 (2004).

[16] A. Lupaşcu, E. F. C. Driessen, L. Roschier, C. J. P. M. Harmans, and J. E. Mooij, Phys. Rev. Lett. **96**, 127003 (2006).

[17] F. Mallet, F. R. Ong, A. Palacios-Laloy, F. Nguyen, P. Bertet, D. Vion, and D. Esteve, Nat. Phys. **5**, 791 (2009).

[18] R. Vijay, D. H. Slichter, and I. Siddiqi, Phys. Rev. Lett. **106**, 110502 (2011).

[19] J. Koch, T. M. Yu, J. Gambetta, A. A. Houck, D. I. Schuster, J. Majer, A. Blais, M. H. Devoret, S. M. Girvin, and R. J. Schoelkopf, Phys. Rev. A **76**, 042319 (2007).

[20] J. A. Schreier, A. A. Houck, J. Koch, D. I. Schuster, B. R. Johnson, J. M. Chow, J. M. Gambetta, J. Majer, L. Frunzio, M. H. Devoret, S. M. Girvin, and R. J. Schoelkopf, Phys. Rev. B **77**, 180502(R) (2008).

[21] A. Houck, J. Koch, M. Devoret, S. Girvin, and R. Schoelkopf, Quant. Info. Proc. **8**, 105 (2009).

[22] M. Steffen, S. Kumar, D. P. DiVincenzo, J. R. Rozen, G. A. Keefe, M. B. Rothwell, and M. B. Ketchen, Phys. Rev. Lett. **105**, 100502 (2010).

[23] M. A. Castellanos-Beltran and K. W. Lehnert, Appl. Phys. Lett. **91**, 083509 (2007).

[24] T. Yamamoto, K. Inomata, M. Watanabe, K. Matsuba, T. Miyazaki, W. D. Oliver, Y. Nakamura, and J. S. Tsai, Appl. Phys. Lett. **93**, 042510 (2008).

[25] B. Yurke and E. Buks, J. Lightwave Technol. **24**, 5054 (2006).

[26] J. Bourassa, J. M. Gambetta, A. A. Abdumalikov, O. Astafiev, Y. Nakamura, and A. Blais, Phys. Rev. A **80**, 032109 (2009).

[27] T. Niemczyk, F. Deppe, H. Huebl, E. P. Menzel, F. Hocke, M. J. Schwarz, J. J. Garcia-Ripoll, D. Zueco, T. Hummer, E. Solano, A. Marx, and R. Gross, Nat. Phys. **6**, 772 (2010).

[28] P. Forn-Díaz, J. Lisenfeld, D. Marcos, J. J. García-Ripoll, E. Solano, C. J. P. M. Harmans, and J. E. Mooij, Phys. Rev. Lett. **105**, 237001 (2010).

[29] J. Bourassa, F. Beaudoin, J. M. Gambetta, and A. Blais, Phys. Rev. A **86**, 013814 (2012).

[30] F. R. Ong, M. Boissonneault, F. Mallet, A. Palacios-Laloy, A. Dewes, A. C. Doherty, A. Blais, P. Bertet, D. Vion, and D. Esteve, Phys. Rev. Lett. **106**, 167002 (2011).

[31] I. Siddiqi, R. Vijay, M. Metcalfe, E. Boaknin, L. Frunzio, R. J. Schoelkopf, and M. H. Devoret, Phys. Rev. B **73**, 054510 (2006).

[32] R. Vijay, M. H. Devoret, and I. Siddiqi, Rev. Sci. Instrum. **80**, 111101 (2009).

[33] M. Boissonneault, A. C. Doherty, F. R. Ong, P. Bertet, D. Vion, D. Esteve, and A. Blais, Phys. Rev. A **85**, 022305 (2012).

[34] E. M. Purcell, Proc. Am. Phys. Soc. **69**, 681 (1946).

[35] A. A. Houck, J. A. Schreier, B. R. Johnson, J. M. Chow, J. Koch, J. M. Gambetta, D. I. Schuster, L. Frunzio, M. H. Devoret, S. M. Girvin, and R. J. Schoelkopf, Phys. Rev. Lett. **101**, 080502 (2008).

[36] D. I. Schuster, A. A. Houck, J. A. Schreier, A. Wallraff, J. M. Gambetta, A. Blais, L. Frunzio, J. Majer, B. Johnson, M. H. Devoret, S. M. Girvin, and R. J. Schoelkopf, Nature **445**, 515 (2007).

[37] A. A. Abdumalikov, O. Astafiev, Y. Nakamura, Y. A. Pashkin, and J. S. Tsai, Phys. Rev. B **78**, 180502 (2008).

[38] M. Boissonneault, J. M. Gambetta, and A. Blais, Phys. Rev. A **77**, 060305 (2008).

[39] M. Boissonneault, J. M. Gambetta, and A. Blais, Phys. Rev. A **79**, 013819 (2009).

[40] C. M. Wilson, G. Johansson, T. Duty, F. Persson, M. Sandberg, and P. Delsing, Phys. Rev. B **81**, 024520 (2010).

[41] G. D. Mahan, *Many Particle Physics*, 3rd ed. (Springer, New York, 2000), p. 788.

[42] E. K. Irish, J. Gea-Banacloche, I. Martin, and K. C. Schwab, Phys. Rev. B **72**, 195410 (2005).

[43] J. Gambetta, A. Blais, M. Boissonneault, A. A. Houck, D. I. Schuster, and S. M. Girvin, Phys. Rev. A **77**, 012112 (2008).

[44] P. Carbonaro, G. Compagno, and F. Persico, Phys. Lett. A **73**, 97 (1979).

[45] A. Lupaşcu, S. Saito, T. Picot, P. C. de Groot, C. J. P. M. Harmans, and J. E. Mooij, Nat. Phys. **3**, 119 (2007).

[46] P. Bertet, F. R. Ong, M. Boissonneault, A. Bolduc, F. Mallet, A. Doherty, A. Blais, D. Vion, and D. Esteve, in *Fluctuating Nonlinear Oscillators*, edited by M. Dykman (Oxford University Press, New York, 2012), p. 1.

[47] P. J. Leek, M. Baur, J. M. Fink, R. Bianchetti, L. Steffen, S. Filipp, and A. Wallraff, Phys. Rev. Lett. **104**, 100504 (2010).

[48] A. Dewes, F. R. Ong, V. Schmitt, R. Lauro, N. Boulant, P. Bertet, D. Vion, and D. Esteve, Phys. Rev. Lett. **108**, 057002 (2012).

[49] A. Dewes, R. Lauro, F. R. Ong, V. Schmitt, P. Milman, P. Bertet, D. Vion, and D. Esteve, Phys. Rev. B **85**, 140503 (2012).

[50] M. Wallquist, V. S. Shumeiko, and G. Wendin, Phys. Rev. B **74**, 224506 (2006).

[51] D. Zueco, P. Hänggi, and S. Kohler, New J. Phys. **10**, 115012 (2008).

[52] M. Scully and M. S. Zubairy, *Quantum Optics* (Cambridge University Press, Cambridge, 1997).